Mechanical tomography of a volcano plumbing system from GNSS unsupervised modeling

François Beauducel[1], Aline Peltier[2], Antoine Villié[3], and Wiwit Suryanto[4]

[1]Institut de Physique du Globe de Paris - Université de Paris
[2]Institut De Physique Du Globe De Paris
[3]Laboratoire de biométrie et biologie évolutive, CNRS, France
[4]Geophysics Research Group, Universitas Gadjah Mada, Indonesia

November 26, 2022

Abstract

Identification of internal structures in an active volcano is mandatory to quantify the physical processes preceding eruptions. We propose a fully unsupervised Bayesian inversion method that uses the point compound dislocation model as a complex source of deformation, to dynamically identify the substructures activated during magma migration. We applied this method at Piton de la Fournaise. Using 7-day moving trends of GNSS data preceding the June 2014 eruption, we compute a total of 15 inversion models of 2.5 million forward problems each, without a priori information. Obtained source shapes (dikes, prolate ellipsoids or pipes) exhibit a global migration from 7-8 km depth to the surface, drawing a "mechanical tomography"? of the plumbing system. Our results allow retrieving geometries compatible with observed eruptive fissures and seismicity distribution, and the retrieved source volume variations made this method a good proxy to anticipate erupted lava in case of no co-eruptive refilling.

Mechanical tomography of a volcano plumbing system from GNSS unsupervised modeling

François Beauducel[1,2], Aline Peltier[1,3], Antoine Villié[4], Wiwit Suryanto[5]

[1]Institut de physique du globe de Paris, Université de Paris, CNRS, F-75005 Paris, France
[2]Institut des Sciences de la Terre, IRD UR 219, Yogyakarta 55166, Indonesia
[3]Observatoire Volcanologique du Piton de la Fournaise, IPGP, F-97418 La Plaine des Cafres, La Réunion
[4]Laboratoire de biométrie et biologie évolutive, CNRS UMR 5558, F-69622 Villeurbanne, France
[5]Geophysics Research Group, Universitas Gadjah Mada, Yogyakarta 55281, Indonesia

Key Points:

- imaging volcano plumbing system from geodesy and mechanical modeling
- detecting precursory magma migration and anticipating real erupted volume
- new unsupervised real-time modeling tool for volcano monitoring

Corresponding author: F. Beauducel, `beauducel@ipgp.fr`

Abstract

Identification of internal structures in an active volcano is mandatory to quantify the physical processes preceding eruptions. We propose a fully unsupervised Bayesian inversion method that uses the point compound dislocation model as a complex source of deformation, to dynamically identify the substructures activated during magma migration. We applied this method at Piton de la Fournaise. Using 7-day moving trends of GNSS data preceding the June 2014 eruption, we compute a total of 15 inversion models of 2.5 million forward problems each, without a priori information. Obtained source shapes (dikes, prolate ellipsoids or pipes) exhibit a global migration from 7-8 km depth to the surface, drawing a “mechanical tomography” of the plumbing system. Our results allow retrieving geometries compatible with observed eruptive fissures and seismicity distribution, and the retrieved source volume variations made this method a good proxy to anticipate erupted lava in case of no co-eruptive refilling.

Plain Language Summary

Imaging the interior of an active volcano and estimating volumes of magma in depth are major challenges of eruption anticipation and forecast. In this work we propose an effective method of data processing that combines a new analytical model of theoretical source, and standard ground deformation measurements, in a fully automated process. The method is sensitive to magma migration and behaves like a scanner that displays a 3D image of the volcano plumbing system.

1 Introduction

Active volcano edifices might deform due to fluid migration and storage into their so-called plumbing system, an interconnected network of internal volumetric substructures like reservoirs, conduits or sills/dikes (Tibaldi, 2015). Indeed, fluid dynamics into the plumbing system involves mechanical constraints (pressure, volume or stress variations) that are applied on the internal boundaries of the medium, inducing deformation and displacements that usually reach the free surface. This behavior highly depends on the medium rheology (Sparks et al., 2019), and deformation intensity can sometimes be much below the instrumental detection capability. Yet, monitoring volcano deformation has been commonly used for more than half a century to detect the subtle warning signals of a volcanic eruption linked to the pressurization of magma body or magma transfers at depth (see Dzurisin (2003) for a complete review and Segall (2010) for limitations of the deformation methods). In this context, the characterization of the magma feeding system (location, volume, shape, etc.) with short-term and reliable quantitative parameters is an important prerequisite for understanding and anticipating any eruptive activity. Inversion of geodetic data with mechanical models has natural capability to locate the pressure source in depth and quantify its characteristics from surface observations (see for instance Toutain et al. (1992); Cayol and Cornet (1998); Beauducel et al. (2004); Anderson et al. (2010); Peltier et al. (2016)). Moreover, any quantitative volcano model needs boundary conditions, in particular those common to the magma fluid dynamics and the volcano mechanical behavior, i.e., the plumbing system geometry. Imaging these structures using various tomography methods has the main goal of describing, in a more quantitative way than any geological approach, the internal structures, which might be used in other geophysical or geochemical dynamic modeling as a priori information.

We propose, in this paper, to follow the magma circulation and/or accumulation by locating and quantifying pressurisation sources in space and time using unsupervised deformation source modeling from GNSS observations at Piton de la Fournaise (PdF). We introduce here the innovative term of “mechanical tomography”, since the method uses magma ascent as an active source that progressively “illuminates” the complex magma plumbing system, and finally gives an image of the internal substructure geometries, which have been activated during the PdF unrest.

PdF (La Réunion Island, Indian Ocean, Figure 1a) is an active basaltic volcano, often in eruption with an average of 2 eruptions per year since 1979, date of the creation of the Observatoire Volcanologique du Piton de la Fournaise (OVPF) from the Institut de Physique du Globe de Paris. The recent eruptive activity mainly occurs inside an uninhabited caldera, called Enclos Fouqué, where a terminal cone topped by two craters (Bory and Dolomieu), gradually built up (Figure 1b).

The location and the shape of the shallow magma reservoirs below the volcano are still debated even if recent geodetic, seismic and geochemical studies converge on a global scheme of a plumbing system constituted of several reservoirs, variably connected and distributed from 10 km depth to the near-surface (Battaglia et al., 2005; Peltier et al., 2009; Di Muro et al., 2014; Boudoire et al., 2019). Passive S and P-wave tomographies made on PdF, using ambient seismic noise and P-wave first arrival times for earthquakes, respectively, show 1) a high S-wave velocity zone from -1 to 1.9 km below the terminal cone interpreted as a preferential paths for magma injections (Brenguier et al., 2007) and 2) a high-velocity plug at sea level, under the summit craters, interpreted as an intrusive, solidified dike-and-sill complex with little fluid magma storage (Prôno et al., 2009). Two low P-wave velocity anomalies, which may highlight magma reservoirs, are found from 0 to 1 km a.s.l. and from 1 to 2 km b.s.l. (Prôno et al., 2009). At greater depth, spatio-temporal distribution of the seismicity located by OVPF may evidence the presence of a deeper reservoir at around 7.5 km depth below the Bory crater (Battaglia et al., 2005; Peltier et al., 2009).

In June, 2014, after an unusual period of 41 months of dormancy, PdF showed signs of unrest with the start of a slow edifice inflation and an increase of the shallow (¡2 km depth) seismic activity on June 9. Two seismic crises (not associated with rapid ground deformation) occurred on June 13 and 17, with 360 and 687 shallow volcano-tectonic earthquakes, respectively. A last seismic crisis that lasted one hour and 16 minutes (888 shallow volcano-tectonic earthquakes located between 0.3 and 1.5 km a.s.l. below the Dolomieu crater; associated with rapid ground deformation) led to an eruption on June 20, 21:35 (UTC time). The eruptive fissures opened on the external and south south-eastern slope of the Dolomieu crater (2348-2480 m elevation; Figure 1b). Eruptive activity ended on June 21, 17:09 (UTC time) and emitted about 0.4±0.2 million m^3 of lava flows (no DRE).

2 Methods

2.1 GNSS Data Processing

Among other multidisciplinary networks, OVPF maintains 24 permanent GNSS stations, one of the densest networks on an active volcano. For this study, we only used the daily solutions of the 10 stations within a 4 km radius from the summit (Figure 1b), where ground displacements have been significant during the June 2014 unrest (Figure 1c). Data shown in the paper were processed using PPP method by the Gipsy-Oasis software (Desai et al., 2014) providing daily solutions in the ITRF2008 referential, with typical standard deviations of 5.2 mm, 4.8 mm, and 11.2 mm for eastern, northern and vertical components, respectively, over 5 years period at a stable station in La Réunion. Horizontal tectonic motion has been removed from the time series using linear trend values of +17.9 mm/yr and +12 mm/yr for eastern and northern components, respectively.

In order to increase the signal to noise ratio of GNSS observations, we compute displacement trends over a 7 days moving-window, which represents a good compromise between the constraint of the source shape and a detailed time tracking of the source. Indeed, as the GNSS daily solutions have relatively high errors, the computation of a linear trend over a few days' sliding sample window increases the sensitivity to detect subtle signals below the error level of individual daily solutions. Typically, the error on a 7-day velocity trend is as low as about 0.14 mm/day, i.e., only 0.8 mm on the displacement.

2.2 pCDM Method

The point compound dislocation model (pCDM) has been proposed by Nikkhoo et al. (2016). It provides analytical expressions for surface displacements due to a source composed of three mutually orthogonal tensile point dislocations, one horizontal and two vertical, freely oriented in space (three rotational degrees of freedom around each 3D axis) in an elastic homogeneous half-space. Original equations depend on nine source parameters: three for the hypocenter location (horizontal coordinates and depth), three volume variations dV_X, dV_Y and dV_Z (of the same sign, for each plane perpendicular to its axis), and three for the angles of rotations ΩX, ΩY, ΩZ (see Figure 2). A tenth parameter is the Poisson's ratio that we fixed to 0.25 to consider an isotropic medium. Since equations use the volume dislocation for the deformation source and not the pressure, the model is independent from other elastic parameters.

In order to express the total volume dislocation ΔV, an easier quantitative parameter for interpretation, we substituted the three volume variations variables with their total value plus two dimensionless shape ratios between 0 and 1, defined as follows:

$$\Delta V = dV_X + dV_Y + dV_Z, \tag{1}$$

$$A = \frac{dV_Z}{\Delta V}, \tag{2}$$

$$B = \frac{dV_Y}{dV_X + dV_Y}, \tag{3}$$

where ΔV is the total volume variation of the source, A is the horizontal over total volume variation ratio, and B is the vertical volume variation ratio.

The pCDM is able to approximate any shape of magma bodies, as dikes, sills, oblate, prolate and other triaxial ellipsoidal shapes (see some examples with corresponding A and B values in Figure 2), and is only relevant at far-field observation points because of the point source approximation. Even if simple, this model is particularly well adapted for real-time monitoring as it gives a first order estimation of the magnitude and shape characteristics of the source(s) at the origin of the surface displacements, and is still easy to implement in an inverse problem.

We also rewrote the original pCDM code in a fully vectorized way (Matlab/GNU Octave and C languages) in order to make it compatible with fast inversion and millions of forward problems. Furthermore, vectorization allows using equations with the varying-depth formulation to approximate the topographic effects (Williams & Wadge, 1998; Beauducel & Carbone, 2015), i.e., adjusting the source depth at each observation point using station elevation above sea level. This method is also a good way to solve the eternal problem of source elevation referencing in half-space models: here the source depths are given in meters b.s.l..

2.3 Inverse Problem

In order to obtain a description as objective as possible of the volcano internal structures at the origin of the surface displacements, we minimize the a priori information and explore the entire space of the nine model parameters using the GNSS trends as observation data. As a first result of this unsupervised inversion method, we represent the model space probability as a function of source location, in order to display all solutions that are consistent with observations (Tarantola, 2006). Identification of a single volume zone with higher probabilities confirms the existence of a cluster of good models, a mandatory condition to possibly select one “best model”.

Since exhaustive grid exploration of the full model space is not reasonable with 9 parameters, we use a Monte Carlo Bayesian parallel algorithm with 5 iterations, each using 500,000 forward problems randomly chosen in the 9-parameters model space, and possible reduction of any parameter search interval between iterations. The aim of this algorithm is to drastically reduce the relevant range of variation for each parameter, with a low probability to exclude the best model. Each iteration performs uniform sampling of the 9 parameters except for horizontal position for which we use a normally distributed sampling centered at the summit with a 5-km standard deviation radius. This a priori information improves the inversion performance as we are expecting source in the neighborhood of the summit area, but does not exclude any possible distant nor deep source location. Then it computes the misfits associated with the created models, using the L1 norm between observed and computed data, and draws the curve representing a proxy of the best possible misfit as a function of the parameter value. If the misfit distribution has a single significant maximum probability mode, the process selects a smaller range for this parameter with higher probability to constrain the best models. This new interval will be used as a starting point for the next iteration. A posteriori uncertainties of the best model solution are given by the interval of variation over each parameter that keeps 68% (one standard deviation) of the highest model probabilities for all the iterations, a total of 2.5 millions forward models.

3 Results

The long-term pre-eruptive edifice inflation is often of very low intensity at PdF (often less than 5 cm; e.g. in (Peltier et al., 2016, 2018), that is why we look at baseline changes (i.e. linear distance between pairs of stations) to better highlight changes in the deformation trend. After 41 months of rest and slow deflation, first signs of edifice inflation at PdF appeared on June 9, 2014 (Figure 1c,d), and accelerated after June 13, with a summit extension well visible on the DSRG-SNEG baseline (see dark red lines in Figure 1d). Intensity of the ground deformation preceding the June 20, 2014 eruption remained particularly low, i.e. less than 1 cm of horizontal cumulative displacements and about 2 cm maximum of vertical cumulative displacements recorded on the summit stations in 11 days. These low intensity of surface observations makes this eruption a good case study for developing sensitive modeling methods.

Results of the inversion modeling on 15 periods (12 before and 3 after the eruption) of 7 day sliding sample window allow retrieving the position and the shape of the pressure source at different times. Figure 3 shows results of each inversion as a full description of the model space probabilities in horizontal and vertical projections (see also Table S1 in the supporting information). Three distinct pre-intrusion phases (phases 1-3) before the final dike propagation to the surface (phase 4) can be distinguished.

1) For the periods spanning June 2-8, 3-9, 4-10 and 5-11, no well-constrained source can be found but probable deep deflation diffuse sources seem to be present below the terminal cone.

2) Inflation sources appeared and became more consistent from the June 6-12 period with a narrower range of models and a best model in inflation located at 4.5 km below sea level, i.e. about 7 km below the summit, with a tilted dike shape. The inflation pressure source, the shape of which evolves from a dike to a pipe, remained deep (0 to 3 km below sea level) until June 16.

3) From the June 11-17 to the June 13-19 periods, when the deformation rate accelerated, the inflation source was shallower, located between 0.7 and 1 km a.s.l. (i.e. be-

tween 1.8 and 1.5 km below the summit). The last pressure source modelled before the eruption, for the period spanning June 13 to June 19, displayed a volume variation of $+210{,}000$ m^3.

4) On June 20, a rapid (1 hour and 16 min of seismic crisis with rapid ground deformation; Figure 1c) and final magma dike injection propagated to the surface and fed the eruption. The shape of the dike appeared in our models only from the June 16-22 sliding-window. For the two previous periods including the beginning of the eruption (June 14-20 and June 15-21), the best models were ellipsoid sources, probably because of the influence of two sources (the pre-eruptive source and the final dike reaching the surface) associated with the integrating effect of the 7-day trend calculation. Volume variations for the two last co-eruptive periods (15-21) and (16-22) were relatively constant, with values of $+230{,}000$ m^3 and $+300{,}000$ m^3, respectively.

4 Discussion

Even with very small ground displacements (less than 1 cm), we are able to image the refilling of the shallow magma plumbing system preceding the June 2014 eruption at PdF. Our previous attempts to detect pre-eruptive magma migration using deformation data may have failed because of the use of too simple isotropic sources as primary models (Beauducel et al., 2014). Success of the inversion using more complex sources may evidence the more frequent deformation sources with flat or elongated shape, like dikes or pipes at PdF.

Our results highlight from June 12 overpressures inside this system at decreasing depth with time (Figure 4), from 7 – 8 km b.s.l. (at the lower limit of our model space) where a reservoir has already been suggested by seismicity in 1998 (Battaglia et al., 2005), to 1.5 km a.s.l., where the shallower reservoir is supposed to lie (1.3 – 1.9 km depth below the summit (Peltier et al., 2016)). Most of the pressure sources below sea level are vertically elongated and seems to highlight the volcano deep conduit connecting the two reservoirs, forming a continuum more or less filled by fluids (Figures 3,4). Rather than following a clear magma migration, which may have required a higher time sampling frequency, we were able to deliver a mechanical tomography of the PdF plumbing system (from about 10 km depth to the surface; Figure 4). The synthetic 3D view of the different sources identified during the June 2014 pre-eruptive unrest evidences a gap at sea level, at the same level where Prôno et al. (2009) describe high-velocity plug interpreted as a solidified complex with little fluid storage, and where Battaglia et al. (2005) describe a discontinuity in the upward migration of the seismicity preceding the 1998 eruption, which occurred after 6 years of rest. In June 2014, no deep seismicity was recorded during the upward magma migration. Following the 1998 eruption, most of the deep recharges were not accompanied by deep seismicity, and the majority of the earthquakes are located above sea level (Lengliné et al., 2016; Duputel et al., 2019). This is the sign of a more or less deep open conduit, which fed the 34 eruptions that occurred between 1998 and 2014 (Roult et al., 2012). Our results show thus the importance of the method we used, which makes it possible to see what seismology does not when the system is already open. Thus, the first models (phase 1) show deep deflation sources before the deep magma migration starts (Figures 3,4). This volume loss might correspond to the emptying of a deeper reservoir(s) before the magma starts to "drill" and follows a path to shallower levels (phase 2; Figure 4). Source locations during phase 3 suggests that the fracturing that allows magma to reach the surface (phase 4) started from about 1.5 km depth below the southern border of the Dolomieu crater (Figures 3,4). The two seismic crises, on June 13 and 17, with earthquakes above sea level, show already shallow pressure source(s) at that time.

The estimated source volume variations are relatively stable during phases 3 and 4, i.e. around 0.25 Mm^3 (see Figure 3) despite the displacement increase over one order of magnitude between pre- and co-eruptive periods. This volume stability makes sense as it might translate a finite volume of magma involved in the last magma migration process. However, when using an isotropic source this process cannot be properly modeled, as for a given depth, the volume variation must be proportional to surface displacements. Using pCDM, the source shape has the capability to be adjusted while keeping a constant volume variation and maintaining a shallow depth. In addition, the final volume variation is of the same order of magnitude as the one obtained using an isotropic source for the whole co-eruptive period (130.000 to 190.000 m^3 (Peltier et al., 2016)), and close to the real erupted volume of 0.4 ± 0.2 Mm^3, i.e. a DRE volume of 0.17-0.28 assuming a porosity range of 30–58% (Di Muro et al., 2014).

In spite of the elastic and homogeneous assumptions of the models, adequacy of the volume variation obtained from deformation and erupted volume seems consistent with the case of short eruptions during which no long-term refilling occurred as for the June 2014 eruption. We demonstrate with our modelling the need of looking at shorter time periods to evidence migration processes and complex internal shallow structures. GNSS daily solutions are certainly a limitation in this context, and higher frequency may help in identification of finer structures.

5 Conclusion

The low intensity of surface observations preceding the June 20, 2014 eruption at PdF makes this eruption a good case study for developing and validating sensitive modeling methods. Our work provides good insights into the refilling of the shallow magma reservoir the days preceding the eruption. The pCDM method we used allows tracking the gradual migration of the magma to the upper reservoir, and the final dike propagation to the surface, by discriminating both the shape, location and volume of the source. The rewriting of the original pCDM code in a fully vectorized way allows for fast inversion and is easy to implement to give first-order modelling results, helpful notably for crisis management. With similar results as obtained at Mt. Etna by Cannavò et al. (2015), our method is fast and fully unsupervised, without a priori information on the source parameters except the choice of the pCDM itself. In view of these promising results, we implemented the method as an extension of the GNSS module in the WebObs system, an integrated web-based system for data monitoring and network management, implemented in 15 observatories worldwide (Beauducel et al., 2020). The module was initially developed with a simple isotropic point source (Beauducel et al., 2014, 2019) and we added the possibility of setting a pCDM source and associated parameters for real-time modeling. This has been especially useful during recent crisis managements (Moretti et al., 2020; Peltier et al., 2020).

Acknowledgments

This work is a tribute to FB's late thesis supervisor François H. Cornet. Authors warmly thank Mehdi Nikkhoo for sharing his revolutionary analytical model. Many thanks to the University of Gajah Mada, the IRD in Jakarta and the Indonesian Ministry RistekDikti for having supported the project. We thank the OVPF staff for high quality data collection. GNSS raw data are available at `http://volobsis.ipgp.fr`, processed data by contacting OVPF-IPGP. WebObs system is an open-source project available at `https://github.com/IPGP/webobs`. This work has been funded by the Observatoire des Sciences de l'Univers de Grenoble and EUROVOLC project that received funding from the European Union's Horizon 2020 research and innovation programme under grant agreement No 731070. IPGP contribution XXXX.

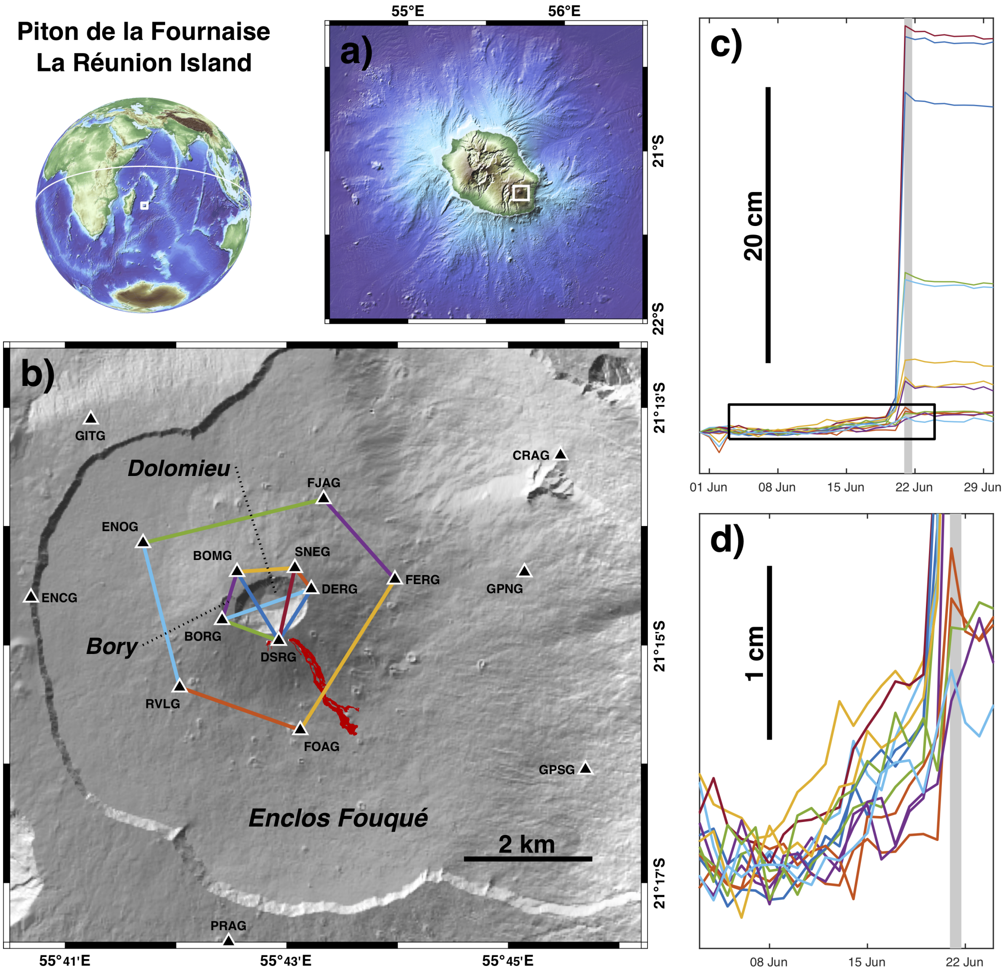

Figure 1. a) Location map of La Réunion Island; b) Zoom on the most active part of Piton de la Fournaise and summit craters. GNSS permanent stations (black triangles), June 2014 lava flows (solid red patch), and selected baselines (color solid lines) are shown; c) baseline variations (i.e. distance changes between pairs of stations) on the pre-, co-, and post-eruptive periods (same colors as in b); d) zoom on the pre-eruptive precursory baseline variations. Grey area indicates eruption time. Topographic data from ETOPO1, SRTM, SHOM, and RGEALTI © IGN 2016.

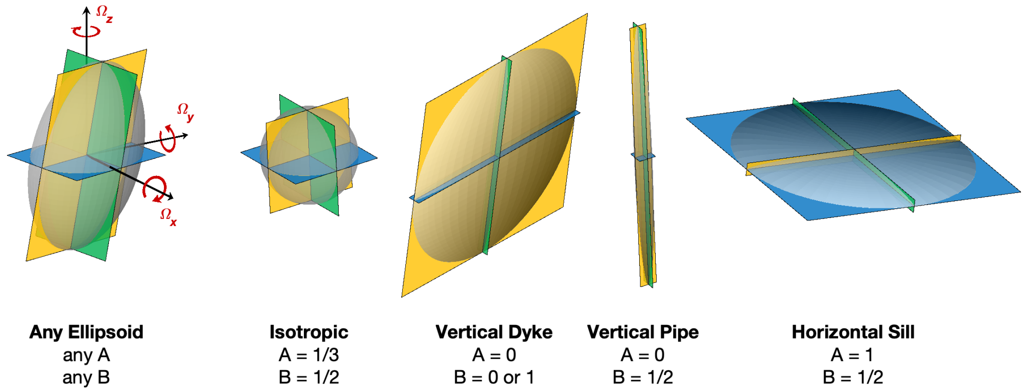

Figure 2. pCDM dislocation plans and rotation angles definition. Example of source shapes and the associated A and B values. Surface of each point dislocation is enlarged to be proportional to its associated volume variation.

References

Anderson, K., Lisowski, M., & Segall, P. (2010). Cyclic ground tilt associated with the 2004–2008 eruption of Mount St. Helens. *Journal of Geophysical Research: Solid Earth*, *115*(B11).

Battaglia, J., Ferrazzini, V., Staudacher, T., Aki, K., & Cheminée, J.-L. (2005). Pre-eruptive migration of earthquakes at the Piton de la Fournaise volcano (Réunion Island). *Geophysical Journal International*, *161*(2), 549–558.

Beauducel, F., & Carbone, D. (2015). A strategy to explore the topography-driven distortions in the tilt field induced by a spherical pressure source: the case of mt etna. *Geophysical Journal International*, *201*(3), 1471–1481.

Beauducel, F., De Natale, G., Obrizzo, F., & Pingue, F. (2004). 3-D modelling of Campi Flegrei ground deformations: An example of trade-off between source and structure. *Pure Appl. Geophys.*, *161*(7), 1329–1344.

Beauducel, F., Lafon, D., Béguin, X., Saurel, J.-M., Bosson, A., Mallarino, D., . . . Fahmi, A. A. (2020). WebObs: The volcano observatories missing link between research and real-time monitoring. *Frontiers in Earth Sciences*, *8*, 48.

Beauducel, F., Nandaka, M. A., Syahbana, D. K., Suryanto, W., Nurnaning, A., Iguchi, M., . . . Komorowski, J.-C. (2019). Real-time magma flux quantization from GNSS as a tool for crisis management. In *VOBP4, Mexico City, November 2019.*

Beauducel, F., Nurnaning, A., Iguchi, M., Fahmi, A. A., Nandaka, M. A., Sumarti, S., . . . Métaxian, J.-P. (2014). Real-time source deformation modeling through GNSS permanent stations at Merapi volcano (Indonesia). In *AGU Fall Meeting Abstracts.*

Boudoire, G., Brugier, Y.-A., Di Muro, A., Wörner, G., Arienzo, I., Metrich, M., . . . Pichavant, M. (2019). Eruptive activity on the western flank of Piton de la Fournaise (La Réunion Island, Indian Ocean): insights on magma transfer, storage and evolution at an oceanic volcanic island. *Journal of Petrology*, *5*.

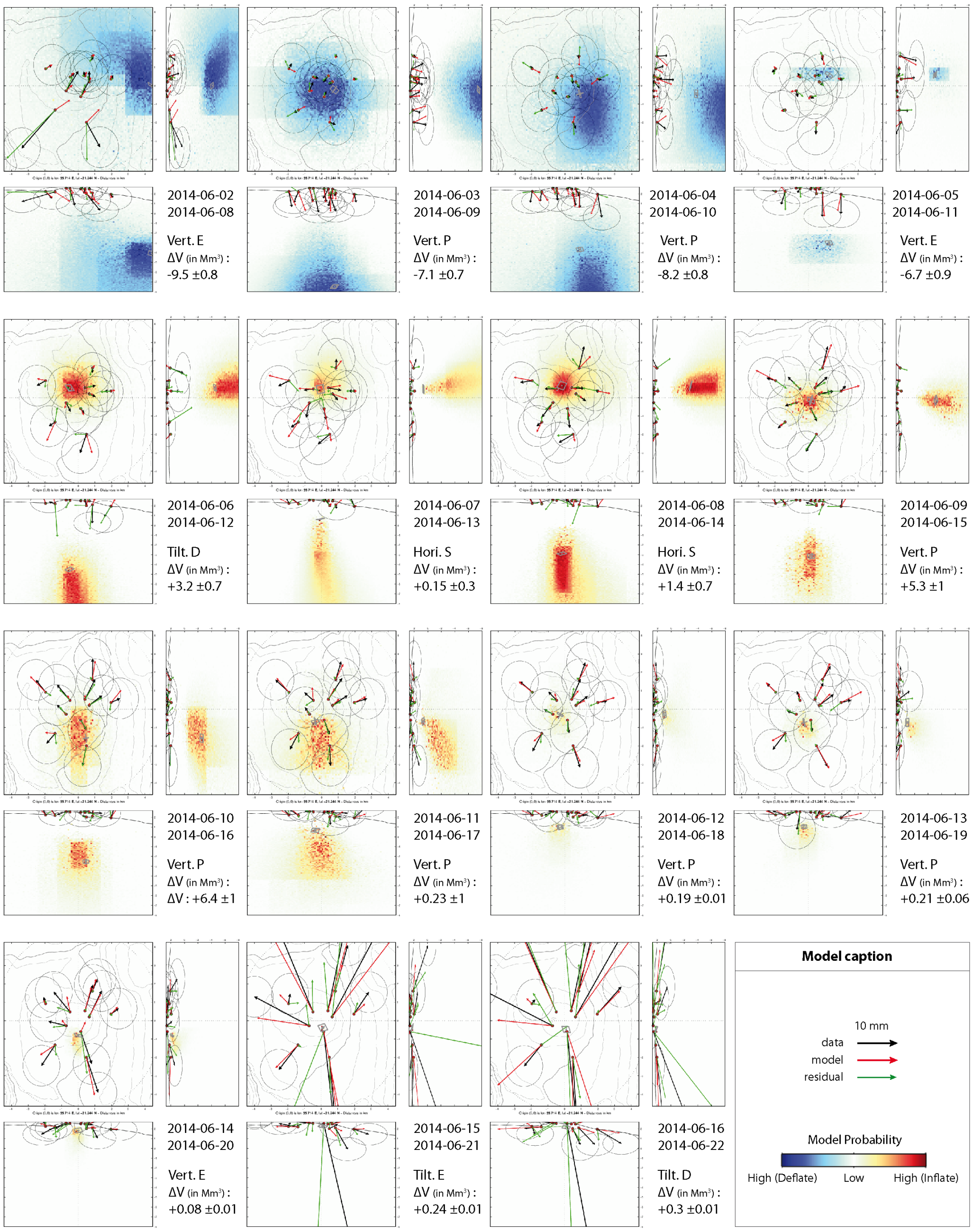

Figure 3. Temporal evolution of the daily pCDM source solution from Bayesian inversion of 7-day displacement trends from June 8 to 22, 2014, in map and vertical cross-section views. Time interval of each model is given in the figure. Color map indicates the maximum probability level combined with the volume variation sign (yellow-orange-red for inflation, green-cyan-blue for deflation). Black, red and green arrows are observed displacements, modeled displacements and residual, respectively. Ellipses are errors. Best model source location and shape are indicated as grey plans, and their source approximate shape (E: Ellipsoid, S: Sill, P: Pipe, D: Dike) and volume variation (Mm^3) are indicated.

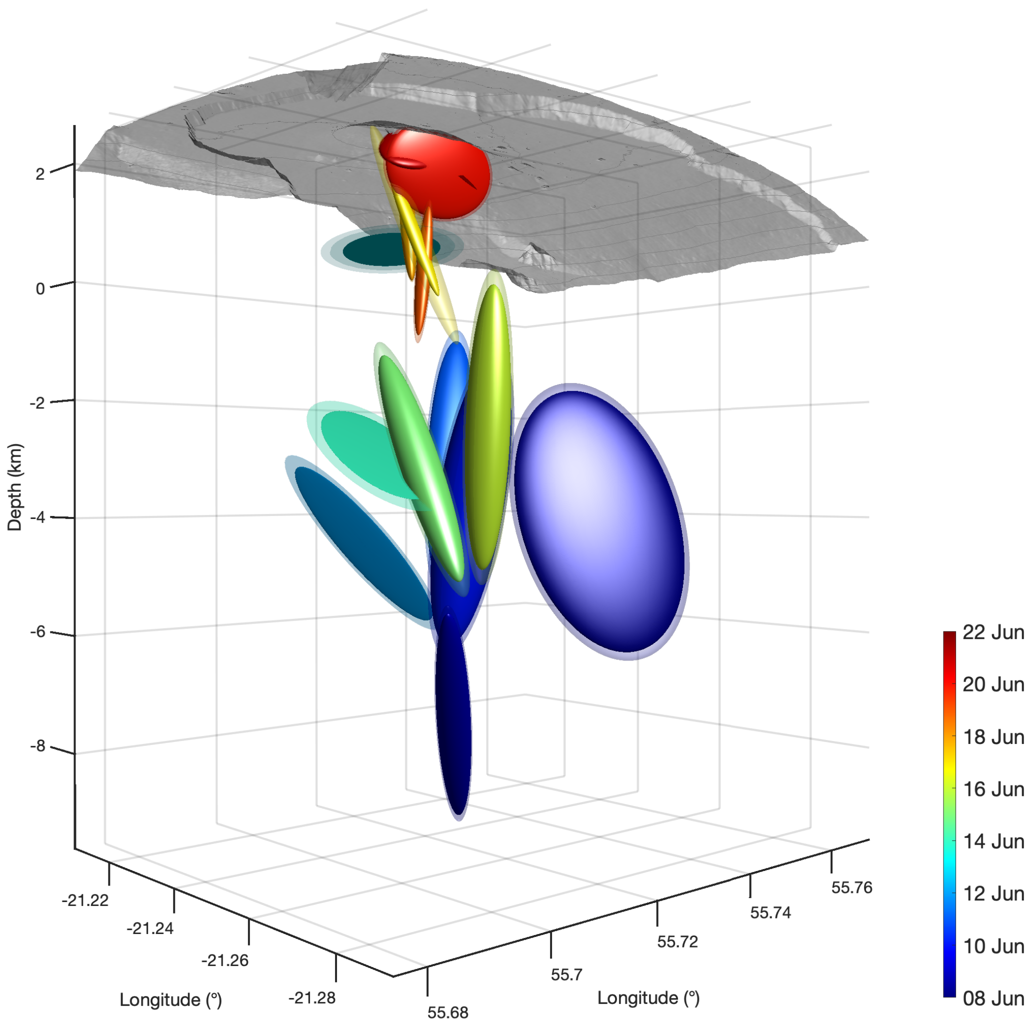

Figure 4. Synthetic and virtual 3D view of the different best models identified during the June 2014 pre-eruptive unrest at Piton de la Fournaise. Colors stand for the most recent date of each time window. Size of each source is proportional to its associated volume variation.

Brenguier, F., Shapiro, N. M., Campillo, M., Nercessian, A., & Ferrazzini, V. (2007). 3-D surface wave tomography of the Piton de la Fournaise volcano using seismic noise correlations. *Geophysical research letters*, *34*(2).

Cannavò, F., Camacho, A. G., González, P. J., Mattia, M., Puglisi, G., & Fernández, J. (2015). Real time tracking of magmatic intrusions by means of ground deformation modeling during volcanic crises. *Scientific reports*, *5*, 10970.

Cayol, V., & Cornet, F. H. (1998). Three-dimensional modeling of the 1983–1984 eruption at Piton de la Fournaise Volcano, Réunion Island. *Journal of Geophysical Research: Solid Earth*, *103*(B8), 18025–18037.

Desai, S., Bertiger, W., Garcia-Fernandez, M., Haines, B., Murphy, D., Selle, C., ... Weiss, J. (2014). Status and plans at the JPL IGS analysis center. In *Intl. gnss service 2014 workshop compendium, ed. igs central bureau* (p. 53).

Di Muro, A., Métrich, N., Vergani, D., Rosi, M., Armienti, P., Fougeroux, T., ... Civetta, L. (2014). The shallow plumbing system of piton de la fournaise volcano (la reunion island, indian ocean) revealed by the major 2007 caldera-forming eruption. *Journal of Petrology*, *55*(7), 1287–1315.

Duputel, Z., Lengliné, O., & Ferrazzini, V. (2019). Constraining spatio-temporal characteristics of magma migration at Piton De La Fournaise volcano from pre-eruptive seismicity. *Geophysical research letters*, *46*(1), 119–127.

Dzurisin, D. (2003). A comprehensive approach to monitoring volcano deformation as a window on the eruption cycle. *Rev. Geophys.*, *41*(1). doi: 10.1029/2001RG000107

Lengliné, O., Duputel, Z., & Ferrazzini, V. (2016). Uncovering the hidden signature of a magmatic recharge at Piton de la Fournaise volcano using small earthquakes. *Geophysical Research Letters*, *43*(9), 4255–4262.

Moretti, R., Komorowski, J.-C., Ucciani, G., Moune, S., Jessop, D., de Chabalier, J.-B., ... Chaussidon, M. (2020). The 2018 unrest phase at La Soufrière of Guadeloupe (French West Indies) andesitic volcano: Scrutiny of a failed but prodromal phreatic eruption. *J. Volcanol. Geotherm. Res.*, *393*, 106769. doi: 10.1016/j.jvolgeores.2020.106769

Nikkhoo, M., Walter, T. R., Lundgren, P. R., & Prats-Iraola, P. (2016). Compound dislocation models (CDMs) for volcano deformation analyses. *Geophysical Journal International*, ggw427.

Peltier, A., Bachèlery, P., & Staudacher, T. (2009). Magma transport and storage at Piton de La Fournaise (La Réunion) between 1972 and 2007: A review of geophysical and geochemical data. *Journal of Volcanology and Geothermal Research*, *184*(1-2), 93–108.

Peltier, A., Beauducel, F., Villeneuve, N., Ferrazzini, V., Di Muro, A., Aiuppa, A., ... Taisne, B. (2016). Deep fluid transfer evidenced by surface deformation during the 2014–2015 unrest at Piton de la Fournaise volcano. *Journal of Volcanology and Geothermal Research*, *321*, 140–148.

Peltier, A., Ferrazzini, V., Di Muro, A., Kowalski, P., Villeneuve, N., Richter, N., ... Gurrieri, S. (2020). Volcano crisis management at Piton de la Fournaise (La Réunion) during the COVID-19 lockdown. *submitted to Seismological Research Letters*.

Peltier, A., Villeneuve, N., Ferrazzini, V., Testud, S., Hassen Ali, T., Boissier, P., & Catherine, P. (2018). Changes in the long-term geophysical eruptive precursors at Piton de la Fournaise: Implications for the response management. *Frontiers in Earth Science*, *6*, 104.

Prôno, E., Battaglia, J., Monteiller, V., Got, J.-L., & Ferrazzini, V. (2009). P-wave velocity structure of Piton de la Fournaise volcano deduced from seismic data recorded between 1996 and 1999. *Journal of Volcanology and Geothermal Research*, *184*(1-2), 49–62.

Roult, G., Peltier, A., Taisne, B., Staudacher, T., Ferrazzini, V., Di Muro, A., &

OVPF, t. (2012). A new comprehensive classification of the Piton de la Fournaise activity spanning the 1985–2010 period. Search and analysis of short-term precursors from a broad-band seismological station. *Journal of Volcanology and Geothermal Research*, *241*, 78–104.

Segall, P. (2010). *Earthquake and volcano deformation.* Princeton Univ. Press.

Sparks, R., Annen, C., Blundy, J., Cashman, K., Rust, A., & Jackson, M. (2019). Formation and dynamics of magma reservoirs. *Philosophical Transactions of the Royal society A*, *377*(2139), 20180019.

Tarantola, A. (2006). Popper, Bayes and the inverse problem. *Nature physics*, *2*(8), 492–494.

Tibaldi, A. (2015). Structure of volcano plumbing systems: A review of multi-parametric effects. *Journal of Volcanology and Geothermal Research*, *298*, 85–135.

Toutain, J.-P., Bachelery, P., Blum, P., Cheminée, J., Delorme, H., Fontaine, L., ... Taochy, P. (1992). Real time monitoring of vertical ground deformations during eruptions at Piton de la Fournaise. *Geophys. Res. Lett.*, *19*(6), 553–556.

Williams, C., & Wadge, G. (1998). The effects of topography on magma chamber deformation models: application to Mt. Etna and radar interferometry. *Geophys. Res. Lett.*, *25*(10), 1549–1552.

Supporting Information for "Mechanical tomography of a volcano plumbing system from GNSS unsupervised modeling"

François Beauducel[1,2], Aline Peltier[1,3], Antoine Villié[4], Wiwit Suryanto[5]

[1]Institut de physique du globe de Paris, Université de Paris, CNRS, F-75005 Paris, France

[2]Institut des Sciences de la Terre, IRD UR 219, Yogyakarta 55166, Indonesia

[3]Observatoire Volcanologique du Piton de la Fournaise, IPGP, F-97418 La Plaine des Cafres, La Réunion

[4]Laboratoire de biométrie et biologie évolutive, CNRS UMR 5558, F-69622 Villeurbanne, France

[5]Geophysics Research Group, Universitas Gajah Mada, Yogyakarta 55281, Indonesia

Contents of this file

1. Table S1

Additional Supporting Information (Files uploaded separately)

1. Caption for Movie S1

Introduction

Table S1 shows all parameters of the best models obtained for the 15 periods of time as used to produce the Figure 4 of the main paper. These models correspond to the best misfit selected from 2.5 millions of computed forward models. See the Figure 3 in the main text to have a better description of the model space for each of the periods.

Movie S1 shows best models in 3D perspective view.

Movie S1.

The short 1 minute length movie shows the best models sources in a 3D perspective view with illuminated topography. The camera position makes two loops around the volume with an additional sinusoidal vertical movement. In the main text, the Figure 4 is a single view selection from the same representation.

Table S1. Summary of the best model deformation sources: time period (days of June 2014), source type (deflation '−' or inflation '+'), source approximate shape as ellipsoid (E), sill (S), pipe (P) or dike (D) and main orientation, coordinates (latitude South, longitude East, in degree), depth b.s.l. (in km), volume variation ΔV (in Mm^3), source geometry (A, B, ΩX, ΩY, ΩZ) and global misfit of the best-fit models at 68.3% confidence for each period we defined.

Time Period	Source Type	Source Shape	Lat. S (deg)	Lon. E (deg)	Depth (km)	ΔV (Mm^3)	A	B	ΩX (deg)	ΩY (deg)	ΩZ (deg)	Misfit (mm)
02-08	−	Vert. E	21.244	55.756	$+4.1 \pm 0.7$	-9.5 ± 0.8	0.07	0.87	−13	−15	+32	5.3
03-09	−	Vert. P	21.246	55.721	$+7.5 \pm 0.4$	-7.1 ± 0.7	0.04	0.56	+36	−2	+38	1.8
04-10	−	Vert. P	21.248	55.723	$+3.7 \pm 0.6$	-8.2 ± 0.8	0.10	0.47	+4	+10	−15	1.9
05-11	−	Vert. E	21.239	55.726	$+3.0 \pm 0.3$	-6.7 ± 0.9	0.02	0.70	−21	+4	+34	2.2
06-12	+	Tilt. D	21.239	55.709	$+4.5 \pm 0.6$	$+3.2 \pm 0.7$	0.93	0.83	−37	+43	−7	4.5
07-13	+	Hori. S	21.240	55.713	-0.6 ± 0.7	$+0.15 \pm 0.3$	0.99	0.34	−4	+19	−10	3.6
08-14	+	Hori. S	21.238	55.712	$+2.9 \pm 0.8$	$+1.4 \pm 0.7$	0.97	0.40	+26	+24	+19	3.3
09-15	+	Vert. P	21.245	55.715	$+3.1 \pm 0.6$	$+5.3 \pm 1.0$	0.07	0.50	−29	−10	+19	2.3
10-16	+	Vert. P	21.258	55.718	$+2.5 \pm 0.4$	$+6.4 \pm 1.0$	0.07	0.44	+4	−1	−9	2.4
11-17	+	Vert. P	21.250	55.710	-0.7 ± 0.6	$+0.23 \pm 1.0$	0.05	0.55	−20	−9	−12	2.1
12-18	+	Vert. P	21.247	55.711	-1.0 ± 0.2	$+0.19 \pm 0.01$	0.06	0.46	−12	−2	+27	1.9
13-19	+	Vert. P	21.251	55.711	-1.0 ± 0.2	$+0.21 \pm 0.06$	0.00	0.43	−1	+8	−14	2.5
14-20	+	Vert. E	21.251	55.714	-1.8 ± 0.05	$+0.08 \pm 0.01$	0.16	0.84	+15	+17	+11	3.6
15-21	+	Tilt E	21.247	55.715	-2.3 ± 0.05	$+0.24 \pm 0.01$	0.66	0.65	+33	−24	−16	49
16-22	+	Tilt D	21.248	55.715	-2.2 ± 0.01	$+0.3 \pm 0.01$	0.87	0.00	+43	−22	+2	76